Comparison of polarity and moment tensor inversion methods for source analysis of acoustic emission data

Comparison of polarity and moment tensor inversion methods for source analysis of acoustic emission data

Caroline C. Graham*, Sergei Stanchits, Ian G. Main and Georg Dresen

Source Analysis of Acoustic Emission Data: A Comparison of Polarity and Moment Tensor Inversion Methods

Caroline C. Graham[a,*], Sergei Stanchits[b], Ian G. Main[a], Georg Dresen[b]

[a]School of Geosciences, University of Edinburgh, Grant Institute, The King's Buildings, West Mains Road, Edinburgh, EH9 3JW, UK.

[b]GFZ German Research Centre for Geosciences, Section 3.2, Telegrafenberg D423, 14473 Potsdam, Germany.

[*]Corresponding author.

1. Introduction

Brittle fracture occurs in the Earth's crust on a wide range of length scales; from the microscopic to the tectonic. The resulting fracture networks are intrinsically related to stress distribution and strongly influence energy transfer within the crust. Energy release along these fractures may be manifested as seismic or acoustic disturbances, which display similar behaviour across this spectrum of scale; for example both earthquakes and acoustic emissions display power law frequency-magnitude distributions [18,25] and Omori Law aftershock behaviour [8]. It follows that to fully understand such systems, we must study them not only on one scale, but also across the transitions between one scale and another. Such work has relevance within the field of seismology and earthquake physics, as well as hydrofracture monitoring within hydrocarbons reservoirs. Furthermore, as the search for new prospects leads to

exploration in increasingly deeper closed-pit mines, so our need to understand fracture system evolution, and the processes that lead to mining-induced earthquakes, likewise increases. This paper describes two techniques used to characterise miroscale fracturing, using acoustic emission data, generated within triaxially compressed granite. These microscopic processes show significant spatial and temporal development up to, and during, the period of macroscopic sample failure. Comparing the results produced by both methods shows that they are consistent with one another and demonstrates the value of the moment tensor inversion approach.

Detailed information relating to fracture network evolution, and the onset of sample failure, can be obtained under controlled conditions during rock fracture experiments. The macroscopic mode by which a rock fails is dependent upon the 'effective pressure', resulting from the applied confining pressure in combination with the pore pressure within the sample. At low effective pressures strain-softening is observed after the peak stress and a loaded rock will fail, by shear localisation, in a brittle fashion. In contrast, at high confinement, strain hardening leads to delocalised flow behaviour [28,29]. This illustrates that rheology does not depend solely upon mean field properties, such as crack density, but also the microscopic processes and feedbacks involved in cracking, how the cracks are organised and how they interact under different external conditions.

In order to understand these effects, we need to have reliable information about the location, geometry and orientations of these cracks, the type of motion associated with them and the evolution of these properties with loading. Whilst samples compressed under brittle conditions will fail in a shear fashion along a macroscopic fault, microscopic analysis indicates that damage by tensile fracture also occurs on the microscale. One such study [10] focused on dry samples of triaxially compressed

Mount Scott granite. Microstructural analysis indicated predominantly tensile microcracks in the early stages of loading, whilst shear fracturing became more intense and spatially concentrated with increasing load.

However, microstructural observations have the disadvantage of only being recoverable after sample unloading and do not provide us with real-time information about microcrack evolution. Alternatively, high frequency pressure disturbances, termed acoustic emissions (AE), which may be recorded during deformation experiments, exhibit a rate of occurrence that is correlated with the inelastic strain rate [13]. These emissions have been attributed to the dynamic release of energy during microcracking events [21,25] and provide us with passively collected information about damage processes occurring within laboratory samples. Such processes can be highly complicated in nature, for instance being related to the collapse of pore spaces and crushing of grains at high confining pressures.

In Ref. [24], a model of fault nucleation and growth in brittle rocks is proposed, based on observations of AE hypocentre distributions and stress-field modelling. They suggest that the nucleation and propagation of faults in granite is a consequence of the interaction of tensile microcracks, prior to the peak stress, within a ‘process zone’. The dilating microcracks lead to changes in the local stress field which, in turn, cause the interaction of cracks to spread unstably, resulting in the propagation of the process zone. As this zone grows, the material yields in a shear fashion within its central part and this creates a 'fault nucleus', which then proceeds to grow behind the process zone as it propagates through the rock. However, as mechanisms and orientations of microcracks were obtained from microstructural analysis, real time data was not available.

Improving our knowledge of these mechanisms is essential in any attempts to understand progression towards brittle failure. Source analysis of AE can elucidate the temporal and spatial evolution of these processes. A number of approaches to the characterisation of laboratory AE sources have been taken. One such technique [12] utilises the distribution of P wave first motions to classify sources coarsely into four categories. A distinction is made between tensile sources and all other AE types, by finding the ratio between up (dilatational) and down (compressional) first motions. A similar method to this [30] assigns an average 'polarity' to each event.

Alternatively a more quantitative approach to AE source analysis is that of moment tensor inversion (MTI), which provides a tensor that describes the forces acting at the source. Such inversion has been widely utilised in the field of seismology, particularly for analysing events with a large non-double-couple component [4,6], such as those observed in volcanically active regions [9,20]. It has the advantage of providing information about, not only the type of motion acting at the source, but also the associated change in volume. One study [5] applied moment tensor inversion to microseismic events recorded in the Underground Research Laboratory (URL) in Pinawa, Manitoba, where a tunnelling operation was underway. They found evidence for failure mechanisms with a non-shear component to them and reported a correlation between the location of a breakout in the tunnel roof and a region of failure mechanisms with a high tensile component. Similarly, [17] inverted for moment tensors from ground motions in two of the South African gold mining districts. He found two very distinct sets of mechanisms; the first, predominantly double-couple in nature, the second, displaying a substantial, coseismic reduction in volume. In addition, moment tensor decomposition has been carried out [22] using AE waveforms recorded during an in situ hydrofracture test. It was shown that sources could be separated into those that

were primarily shear in nature and those with a significant tensile component.

Inversion of laboratory AE data for moment tensors has also been carried out for material deformation experiments. For example, [26] utilised moment tensor analysis to characterise microcracking events in unconfined mortar and concrete plates. They determined crack types, orientations and volumes using this method and demonstrated a technique for damage evolution estimation from moment tensor data. AE source analysis by moment tensor inversion has also been applied successfully to other laboratory media, including salt rock [3,15-16], granite and marble [2].

Whilst a number of source analysis techniques have been proposed for AE laboratory data, the authors are unaware of any studies applying and comparing inversion with other approaches, whilst utilising the same data set. This study compares the application and results of two methods of first motion analysis and source classification, using AE data collected during the triaxial compression of granite in the brittle regime. It is a polarity technique [30] and the 'simplified green's function moment tensor analysis' [22], which are compared in this study. The former, is a simple method for estimating the predominant source movement, based on the mean polarity of the first motions recorded across an array of AE sensors. Whilst this approach is simple and fast, it can only provide limited information about the source type. The latter, approach is a moment tensor inversion method that utilises first motion amplitudes to invert for a moment tensor. The tensor can then be decomposed and classified depending on the predominance of its constituent parts. This technique has the advantage of providing more detailed information about the different components of and orientation of source mechanisms. A more detailed description of the methods used is given in section 3 (below). In this study we compare the results of these two techniques using the same

data set, in order to test the robustness and value of both an inversion approach and a more simplified method.

2. Experimental technique

In this section, sample selection, characteristics and preparation are discussed. This is followed by a description of the experimental set-up, the data acquisition system and the method of location of acoustic emission hypocentres.

2.1 Sample description

Due to the large number of acoustic emissions produced in laboratory experiments, their classification into specified source mechanisms relies on selecting generalised categories into which, in reality much more complicated, microscale events are placed. Rock types with a significant porosity will exhibit dilatant behaviour, shear localisation and compaction during compressional loading. For the purposes of this study, a low porosity crystalline rock, in this case a granite, was utilised so as to focus primarily on the two former processes.

The rock used in this work is a red granite, sourced from Aue, Erzgebirge, Germany. It is composed of 30% quartz, 40% plagioclase, 20% K feldspar and 10% mica (Zang et al., 1998). The grain size within this rock type varies between 0.9 and 1.8mm, with an average value of 1.3mm. Porosity was measured as 1.3% and the Poisson's ratio was estimated as 0.17. A cylindrical sample was used with a length, l, of 125mm and

diameter, *d*, of 50mm, giving a ratio *l*/*d* of 2.5. The sample failed in a brittle fashion at a confining pressure of 20MPa, with relatively localised damage. The resulting fault trace was orientated at an angle of approximately 30º from the maximum compressive stress (Figure 1a).

2.2 Equipment set up

A servo-operated MTS 4600kN loading frame (MTS Systems Corporation 1996) was used to apply the maximum stress to a cylindrical sample of red Aue granite. The surrounding hydraulic oil within the pressure vessel, provided a confining pressure of 20MPa to the sides of the cylinder whilst the sample was protected in a rubber jacket. Eleven piezoelectric crystal transducers (PZT) were contained within brass housings with conformably shaped bases, so as to give a tight contact with the sample. These housings were then bonded to the sample surface with epoxy in the arrangement shown in Figure 1b. The transducers, with a frequency range of 0.1-2MHz, provided acoustic emission waveforms, which were then subjected to an amplification of 40dB by Physical Acoustics Corporation preamplifiers. The waveforms were then digitised and recorded by a 16 bit data acquisition system (DaxBox, Prökel GmbH). Following [14], the rate of acoustic emissions was used as a feedback control for the press, thereby drawing out the length of the failure process and allowing a greater number of the AE to be successfully located, up to and during the post-peak stress phase.

Variations in P-wave velocity were monitored during loading by applying an electrical pulse to three PZTs at minute intervals. The resulting arrival times and amplitudes were then recorded at each sensor in the array, allowing vertical and horizontal velocities to

be determined for a number of different regions within the sample. A more detailed account of the setup for this experiment can be found in Ref. [27].

2.3 Event Location

Source location was based on automatic picking of P-waves for a minimum of eight sensors. After selection of P-wave arrival times, hypocentre determination was carried out automatically using an algorithm based on the downhill simplex algorithm [19]. The resulting location precision was estimated at ±2.5mm.

3. Methodology

After successful location of events was carried out, two different techniques for characterising and classifying sources were applied to the data. The first method used is that of [30], where events are classified according to the polarity of the first motions at each sensor. The second approach involves a full moment tensor inversion, the methodology for which is described by [22]. In this section, a description of both of these approaches is given.

3.1 Polarity technique

The polarity classification method used in this study is described by [30]. Here, the first motion amplitude, A_i, at k sensors, is used to find an average polarity for each event,

according to:

$$pol = \frac{1}{k}\sum_{i=1}^{k} sign(A_i) \quad (1)$$

This provides us with an estimate of the net polarity of the volume change at the location of the source. Classification is then carried out within three selected ranges, which are ascribed to the formation of different types of microcracks. AE are described as S-type events (shear) for a polarity between -0.25 and +0.25, T-type (tensile) for pol<-0.25, or C-type (collapse) for pol>+0.25. Once sources have been classified, the best-fitting double-couple total mechanism can be fitted to the first motion amplitudes for those events identified as shear. Orientations of shear fractures can then be determined from the resulting focal mechanisms [30], as they should correspond to one of the two nodal planes. This assumption (pure double-couple) is analogous to the typical focal mechanism in earthquake seismology, prior to the digital era. For natural tectonic seismicity it is often a very good assumption. However, this is not the case for laboratory or mining-scale induced events.

3.2 Moment tensor inversion technique

Moment tensor inversion has been regularly applied in the field of seismology, since the advent of digital recordings, and allows analysis of the mechanism acting at the source of the earthquake [4,6]. The source is represented as a 3 by 3 matrix, known as the moment tensor, **M**, which is a function of the orientation and size of the source. Each element in the array represents one of 9 force-couples acting at the source. To conserve

angular momentum **M** is symmetric and, therefore, contains six independent elements; 3 tensile or compressional couples along the diagonal and a remaining 3 shear couples off the diagonal. The scalar moment M_0 gives us the magnitude of the moment tensor and is the product of the shear modulus, μ, rupture area, A, and average scalar slip on the fault, $\bar{u}$, (eq. 2).

$$M_0 = \mu \bar{u} A \tag{2}$$

The full moment tensor describes a range of source types that include shear, tensile, mixed-mode and compaction events. A number of methods have been developed to invert for these elements from seismic waveforms, using arrival times and amplitudes of, generally, several seismic phases.

However, for acoustic emission waveforms the effects of reflections and ringing within the sample often lead to a complicated coda, or tail, to the seismograms, where shear and surface waves / normal modes are not readily distinguishable. Therefore, any moment tensor inversion based on laboratory measurements should, preferably, require only P-wave data; the only reliable phase. If the double-couple approximation holds (i.e. the source is pure or simple shear) then there will be no volumetric change at the source and the trace of **M** will be zero. For macroscopic earthquakes, the volumetric component is rarely distinguishable from zero. However, microstructural analysis of experimentally deformed rock samples, regularly demonstrates that such sources can be much more complicated than most earthquake sources and are often associated with a significant volume change. A great advantage of moment tensor inversion of AE is that it determines a volumetric component, where one exists above the detection limit. Furthermore, unlike some techniques, it can provide information on the orientation of

all sources.

Standard elastic wave theory [1] allows us to express the elastic displacement **u**(**x**,t), recorded at position **x** and time *t* and due to a displacement continuity **b**(**y**, t) at position **y**, as a function of the moment tensor **M**. Let us consider **M** to be the product of the initial discontinuity and the elastic constants of the medium, such that;

$$M_{pq} = C_{pqkl} b_k n_1 \,, \tag{3}$$

where **n** is the normal vector, defined positive outward from the surface of the crack. We can then represent the resultant waveform as;

$$u_i(\underline{x},t) = G_{ip,q}(\underline{x},\underline{y},t) M_{pq} * S(t) \,, \tag{4}$$

where the product of **M** and the spatial derivative of the associated Green's functions, is convolved with the source-time function *S(t)*. The Green's function describes the impulse response of the medium to a spike, measured at location **x** on the sample boundary. In the SiGMA method [22,23], only the P-wave part of the full-space Green's function is selected, allowing for a simplification of the problem when applied to an isotropic, homogenous medium. We are then left with an equation for P-wave amplitude, dependent upon **M**, but not upon time;

$$A(\underline{x}) = \mathrm{Ref}(\underline{t},\underline{r}) \cdot DF / (4\pi\rho R v_p^3)(r_1, r_2, r_3) \begin{pmatrix} m_{11} & m_{12} & m_{13} \\ m_{12} & m_{22} & m_{23} \\ m_{13} & m_{23} & m_{33} \end{pmatrix} \begin{pmatrix} r_1 \\ r_2 \\ r_3 \end{pmatrix} \tag{5}$$

Here, A is the displacement produced by an AE source (Fig. 2a) at point **y** and recorded at a position, **x**, which is a distance *R* away, in a direction $\mathbf{r} = (r_1, r_2, r_3)$. It is important to note that in the notation of [22], **t** above is not time but the direction of AE sensor sensitivity, such that *Ref(t, r)* is the reflection coefficient at the observation surface. In addition, ρ is the density of the medium, v_p is the P-wave velocity and *DF* is the crack area. With observations of P-phase amplitudes from six or more receivers, it is therefore possible to solve for the unique moment tensor elements. In Ref. [22] Ohtsu argues that, since they are not dependent upon time, the resulting solutions are inherently stable.

Once the moment tensor of a source has been found, decomposition can be carried out using its eigenvalues ($\lambda_{max}, \lambda_{int}, \lambda_{min}$), to resolve the double-couple (DC) and non-double couple (NDC) parts of the source (Fig. 2b). For example [11], the tensor be split into a double-couple (DC) component, an isotropic component (ISO) and a deviatoric or 'Compensated Linear Vector Dipole' component (CLVD). In Ref. [22] the maximum shear and CLVD components are defined as *X* and *Y* respectively, giving a DC part (*X*, 0, -*X*) and a CLVD part (*Y*, -0.5*Y*, -0.5*Y*). This leaves the remaining isotropic part in all directions, *Z*. The relative proportions of *X*, *Y* and *Z* can then by found by first normalizing with respect to the maximum eigenvalue, such that;

$$\lambda_{max} / \lambda_{max} = 1 = X + Y + Z \tag{6}$$

and then solving simultaneously with;

$$\lambda_{int} / \lambda_{max} = 0 - 0.5Y + Z \tag{7}$$

$$\lambda_{min} / \lambda_{max} = -X -0.5Y + Z \quad (8)$$

Hence, values of X=0, Y+Z=1, would represent an entirely tensile source, whilst a purely shear source would lead to X=1 and Y=Z=0. Sources can then be classified using criterion suggested and tested by [23]; for X>60% the source is considered to be predominantly shear, for X<40% it is classified as tensile and for 40%<X<60% it is termed 'mixed-mode' in nature, having both significant shear and tensile components.

Finally, in this study the trace of the moment tensor was used to find those events leading to a net loss in volume, which are classified as 'collapse' sources. It should, however, be noted when interpreting the results that this, by definition, excludes collapse sources with a significant CLVD component, which lead to no net change in volume. There also remains the possibility of some aseismic component to a source, which cannot be determined. However, the major advantage of the moment tensor technique is that the associated eigenvectors can then be used to obtain crack opening directions for *all* source types. Having the full tensor also allows detailed comparison of the inferred fracture or fault directions with microstructural data, or principal components with applied strain direction.

4. Results

4.1 Spatial progression of fracture

Triaxial compression was carried out on a cylindrical sample of red Aue granite with AE feedback controlling loading rate. The peak differential stress applied during the

test was 365MPa and failure occurred just before 7000s, along a macroscale fault plane with an orientation of approximately 30º to the maximum principal stress. During this process a very significant increase in the rate of acoustic emissions was observed before failure. Figure 3 shows the loading curve for the experiment and the variation in the vertical and horizontal P-wave velocities through the sample, V_{ax}, V_{h1}, V_{h2}, V_{h3}, respectively.

Hypocentre locations (Figures 4 & 5) of large magnitude events, from different time windows during the loading process, show a progressive change from diffuse (stage a) to more localised (stage b) AE-associated damage, concentrated near the eventual macroscopic fault plane. Localised fracturing starts at the side of the cylinder, and progresses towards its bottom corner during failure. It should be noted that the uncertainty in source location is clearly visible, as some events are located out with the sample box. The variation in event locations and source types are shown for both the polarity (Fig. 4a-c) and MTI methods (Fig. 5a-c). Both indicate a significantly higher proportion of tensile to shear events in the initial loading phase, followed by an increase in microshearing over time. Only shear and tensile sources are shown here for clarity, but other events were also classified as collapses (both techniques) or mixed-mode sources (MTI only). It should also be noted that both techniques indicate a degree of tensile activity within the failure zone, even during the final stages of loading. This is consistent with observations of a dynamic dilation 'suction pump' mechanism for fluid flow observations during slip [7].

4.2 Temporal variation of sources

Due to the large number of AE events produced during loading of the Aue granite, the

source mechanisms were analysed in terms of temporal variation in the relative proportions of each mechanism type. After events were classified into different source types, a rolling average of the number of events for each source type was calculated, for every hundred events and with a quarter overlap between windows. As the inversion process requires a number of events to be discarded, due to the lack of a well-fitting solution, the number of events for each source type was normalised by the total number of events within each window. The resulting plots (Fig. 6 & 7), derived from both the polarity and MTI classifications have many similarities. Both techniques clearly show that, during the early stages of acoustic emission (stage a), predominantly distributed tensile motion is the preferred mode of fracture on the microscopic scale. However, close to peak strength (stage b), a change to primarily shear microfracture, localised near the eventual fault plane, is also observed. Similar findings have been reported in a number of other studies [24,27].

Figures 8 & 9 show the similarity between the resulting source type variability determined by both methods, with tensile sources initially dominating, before being superseded by shear sources. The results for the behaviour of shear sources are particularly similar, and this may be a reflection of the simplicity of the source type. In other words, a relatively shear dominant source is more common than a relatively tensile dominant source. In addition, the peak in tensile events in Fig 8 is somewhat smaller for the MTI method, and is attributed to the addition of a 'mixed-mode' source type, with both a significant shear and tensile component. Whilst the gradient in the variation in MTI tensile events is shallower, the general trends are still very similar in both Figures 6 and 7. In addition, the percentage of 'collapse' type sources is somewhat smaller in the MTI case, as is discussed below (section 5.1).

5. Discussion

5.1 Physical Mechanisms

Whilst we can separate sources into different classes, using either of the techniques described in this paper, we must also consider the physical mechanisms that generate such signals before attempting to utilise the results. In the case of the average polarity technique, we must be aware that we cannot necessarily, for example, differentiate between a shear source with no tensile component and a shear with a small tensile component. Equally, C-type events that are described as 'collapse' mechanisms are sources containing a predominant collapse component, yet they will also require shearing between grains to be physically achievable in reality. Conversely, the moment tensor technique allows those events with an implosive net volume change to be identified as collapse sources, by using the trace of M. As a consequence, we would expect the average polarity technique to classify somewhat different proportions of event types. Additionally, the presence of a third class of source, the mixed-mode type, in the MTI method must reduce the percentage of shear or tensile sources that are identified. This illustrates the advantages of the full moment tensor technique for discriminating in more detail between competing microstructural processes.

5.2 Comparison of the two techniques

The results of this study are encouraging for the field of AE source analysis. When applying two dissimilar techniques to an AE laboratory data set, we see a concurrent set

of results from both methods. For large datasets, finding the average polarity of events provides a quick and simple method to analyse sources, demonstrating similar results, albeit less informative results, to the full moment tensor inversion. Unlike the polarity technique of [30], the SiGMA approach may not always produce a solution, as it is more sensitive to issues such as the uncertainty in source location. This uncertainty is of the order of ±2.5mm, meaning that it is possible for an event near the sample edge to be located out with the cylinder. However, where a solution is achievable, MTI provides far greater amounts of information about the source involved, such as orientations of non-DC events and full description of the source in terms of its 6 independent force couples. In addition, moment tensors provide a description of the volumetric change at the source and can be used to sum up AE-associated damage within the rock, during the loading process [2,26]. Such an approach is clearly a powerful tool when investigating damage progression, in terms of the characteristics, organisation and evolution of microcracking.

One of the major challenges within this field is that of processing increasing amounts of data. In order to overcome this during analysis, sources must be over-simplified, by being placed into a number of broad categories. Microstructural analysis indicates that the reality is far more complicated. Further work into the nature of such sources in different media and under different laboratory conditions is, therefore, required.

6. Conclusions

Temporal and spatial changes in acoustic emissions in rock deformation experiments can elucidate the processes that produce microseismic events in the earth, such as those

observed in mining structures and hydrocarbons reservoirs. In order to properly understand the evolution of these changes, the microscale mechanisms involved must also be considered. This can, in part, be done by analysing experimentally produced AE sources. A number of techniques have been applied in this way, but with very little comparison between methods. In this study, two different methods were applied to the same data set in order to make such a comparison; one based upon polarity of first motions, the other involving a moment tensor inversion from the amplitudes of the first motions.

Sources were located, analysed, classified and their varying proportions plotted against time. Whilst the categories that sources were sorted into, for each technique, are somewhat different in their meaning, the results are still encouragingly similar. Both indicate that for this data set, produced during the triaxial compression of a granite, tensile sources dominate during the early stages of loading, but are superseded by shear sources prior to failure. These results suggest that both the average polarity and SiGMA methods provide useful information about the characteristics of AE sources and, hence, the associated damage within a deforming rock. We conclude that source analysis of acoustic emissions, and moment tensor inversion in particular, show significant potential for characterising and elucidating the processes involved in brittle damage in laboratory rock fracture tests.

Acknowledgements

This work was funded by the National Environment Research Council, award no: NER/S/S/2005/13745. We would like to thank Mitsuhiro Shigeishi and Masayasu

Ohtsu for granting us access to their inversion code, SiGMA.

References

[1] Aki K., Richard P.G. Quantitative Seismology. University Science Books; 2002.

[2] Chang S.-H., Lee C.-I. Estimation of cracking and damage mechanisms in rock under triaxial compression by moment tensor analysis of acoustic emission. Int J Rock Mech Min Sci 2004;41:1069-1086.

[3] Dahm T., Manthei G., Eisenblatter J. Automated moment tensor inversion to estimate source mechanisms of hydraulically induced micro-seismicity in salt rock. Tectonophysics 1999;306:1-17.

[4] Dziewonski A.M., Chou T.-A., Woodhouse J.H. Determination of earthquake source parameters from waveform data for studies of global and regional seismicity. J Geophys Res 1981;86(B4):2825-2852.

[5] Feignier B., Young P. Moment tensor inversion of induced microseismic events: evidence of non-shear failures in the -4 < M <-2 moment magnitude range. Geophys Res Lett 1992;19(14):1503-1506.

[6] Frohlich C. Characteristics of well-determined non-double-couple earthquakes in the Harvard CMT catalog. Phys Earth and Planet Inter 1995;91:213-228.

[7] Grueschow, E., Kwon, O., Main, I. G., Rudnicki, J. W. Observation and modeling of the suction pump effect during rapid dilatant slip. Geophys Res Lett 2003;30(5):1226.

[8] Hirata T. Omori's Power law aftershock sequences of microfracturing in rock fracture experiment. J Geophys Res 1987;92(B7):6215-6221.

[9] Julian B.R. Evidence for dyke intrusion earthquake mechanisms near Long Valley caldera, California. Nature 1983;303:323-325.

[10] Katz O., Reches Z. Microfracturing, damage, and failure of brittle granites. J Geophys Res 2004;109(B01206).

[11] Knopoff L., Randall M.J. The compensated linear-vector dipole: a possible mechanism for deep earthquakes. J Geophys Res 1970;75(26):4957-4963.

[12] Lei X., Kusunose K., Rao M.V.M.S., Nishizawa O, Satoh T. Quasi-static fault growth and cracking in homogeneous brittle rock under triaxial compression using acoustic emission monitoring. J Geophys Res 2000;105(B3):6127-6139.

[13] Lockner D. The role of acoustic emission in the study of rock fracture. Int J Rock Mech Min Sci & Geomech Abstr 1993;30(7):883-899.

[14] Lockner, D. A., Byerlee, J. D., Kuksenko, V., Ponomarev, A., Sidorin, A. Quasi-static fault growth and shear fracture energy in granite. Nature 1991;350:39-42.

[15] Manthei G. Characterization of acoustic emission sources in a rock salt specimen under triaxial compression. Bull Seismol Soc Am 2005;95(5):1674-1700.

[16] Manthei G., Eisenblatter J., Dahm T. Moment tensor evaluation of acoustic emission sources in salt rock. Constr & Build Materials 2001;15:297-309.

[17] McGarr A. Moment tensors of ten witwatersrand mine tremors. Pure Appl Geophys 1992;139(3/4):781-800.

[18] Meredith P.G., Main I.G., Jones C. Temporal variations in seismicity during quasi-static and dynamic rock failure. Tectonophysics 1990;175:249-268.

[19] Nelder J.A., Mead R. A simplex method for function minimization. Computer J 1965;7(4):308-313.

[20] Nettles M., Ekstrom G. Faulting mechanism of anomalous earthquakes near Bardarbunga Volcano, Iceland. J Geophys Res 1998;103(B8):17973-17983.

[21] Ohnaka M., Mogi K. Frequency charactersitics of acoustic emission in rocks under uniaxial compression and its relation to the fracturing process to failure. J Geophys Res 1982;87(B5):3873-3884.

[22] Ohtsu M. Simplified moment tensor analysis and unified decomposition of acoustic emission source: application to in situ hydrofracture test. J Geophys Res 1991;96(B4):6211-6221.

[23] Ohtsu M. Acoustic emission theory for moment tensor analysis. Res Nondestructive Eval 1995;6(3):169-184.

[24] Reches Z., Lockner D.A. Nucleation and growth of faults in brittle rocks. J Geophys Res 1994;99(B9):18,159-18,173.

[25] Scholz, C.H. The frequency-magnitude relation of microfracturing in rock and its relation to earthquakes. Bull Seismol Soc Am 1968;58(1):399-415.

[26] Shigeishi M., Ohtsu M. Acoustic emission moment tensor analysis: development for crack identification in concrete materials. Constr & Build Materials 2001;15:311-319.

[27] Stanchits S., Vinciguerra S., Dresen G. Ultrasonic velocities, acoustic emission characteristics and crack damage of basalt and granite. Pure Appl Geophys 2006;163:974-993.

[28] Wong T.-f., Szeto H., Zhang J. Effect of loading path and porosity on the failure mode of porous rocks. Appl Mech Rev 1992;45(8):281-293.

[29] Wong T.-f., David C., Shu W. The transition from brittle faulting to cataclastic flow in porous sandstones: mechanical deformation. J Geophys Res 1997;102(B2):3009-3025.

[30] Zang A., Wagner C., Stanchits S., Dresen G., Andresen R., Haidekker M.A. Source analysis of acoustic emissions in Aue granite cores under symmetric and asymmetric compressive loads. Geophys J Int 1998;135:1113-1130.

Figure Captions

Figure 1 a.) Aue granite sample after failure and unloading (125mm height).

b.) Projected sample surface showing position of AE sensors during testing. Sensors 1, 4, 5, 8 and 9 were used as transmitters for ultrasonic velocity measurement.

Figure 2 a.) Source-receiver geometry assumed for the moment tensor inversion

b.) Idealised acoustic emission sources and their associated focal mechanisms.

Figure 3 Differential stress applied to the sample during the course of the experiment. P-wave velocities are also shown for three horizontal zones (Vh1, Vh2, Vh3) and the axial P wave velocity (Vax). Three stages (a-c) of the loading process are highlighted.

Figure 4 a-c.) Hypocentre locations for granite sample, Ag72r. Source types are shown as derived by the average polarity technique. Predominantly shear and tensile source types are indicated by open circles and closed triangles respectively. Symbol size is directly related to event magnitude and small magnitude events are not shown, for clarity. Slices are through the Y-Z plane during different time intervals; a.) 3000-6000s (stage a), b.) 6000-7000s (stage b), c.) 7000-8620s (stage c). The inner rectangle denotes the location and size of the sample.

Figure 5 a-c.) Hypocentre locations for granite sample, Ag72r. Source types are shown as derived by moment tensor inversion. Predominantly shear and tensile source types are indicated by open circles and closed triangles respectively. Symbol size is directly related to event magnitude and small magnitude events are not shown, for clarity. Slices are through the Y-Z plane during different time intervals; a.) 3000-6000s (stage a), b.)

6000-7000s (stage b), c.) 7000-8620s (stage c). The inner rectangle denotes the location and size of the sample.

Figure 6 Temporal variation in source type dominance, as classified by the average polarity method.

Figure 7 Temporal variation in source type dominance, as classified using moment tensor inversion.

Figure 8 Variations in the proportion of tensile to total number of AE events. The dotted line and crosses represents results of the average polarity method. The straight line and circles indicate the results for moment tensor inversion.

Figure 9 Variations in the proportion of shear to total number of AE events. The dotted line and crosses represents results of the average polarity method. The straight line and circles indicate the results for moment tensor inversion.

Figure 1 BW

a.)

b.)

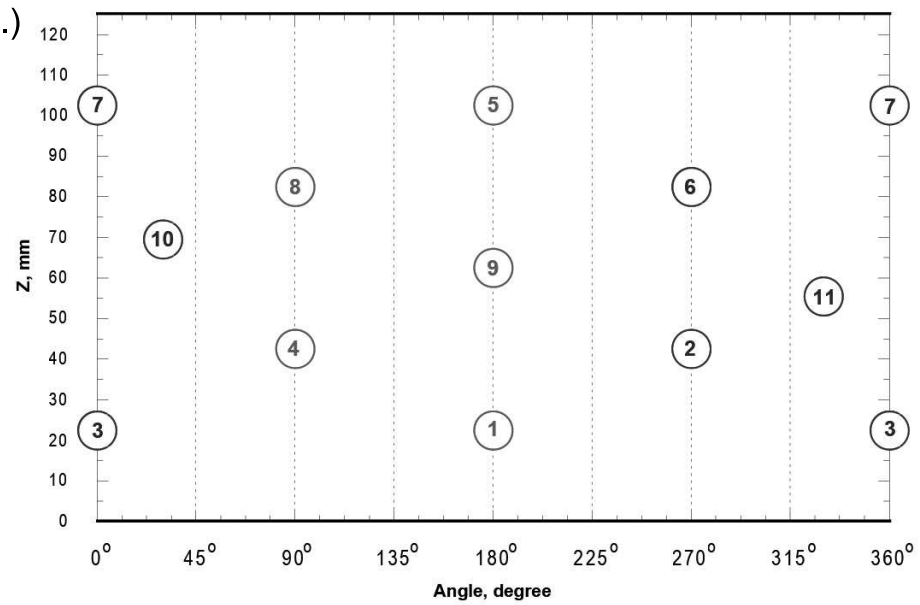

Figure 2 BW

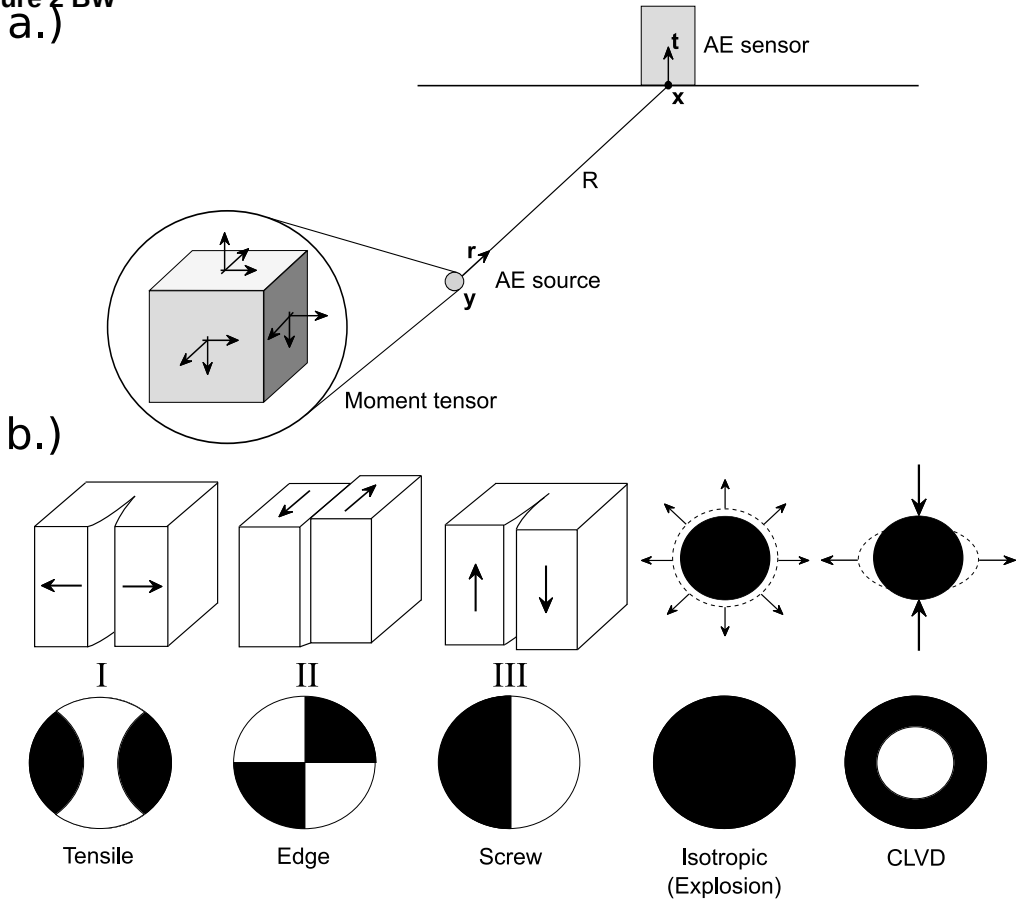
a.)
t
AE sensor
x
R
r
AE source
y
Moment tensor
b.)
I
II
III
Tensile
Edge
Screw
Isotropic
(Explosion)
CLVD

Figure 3 BW

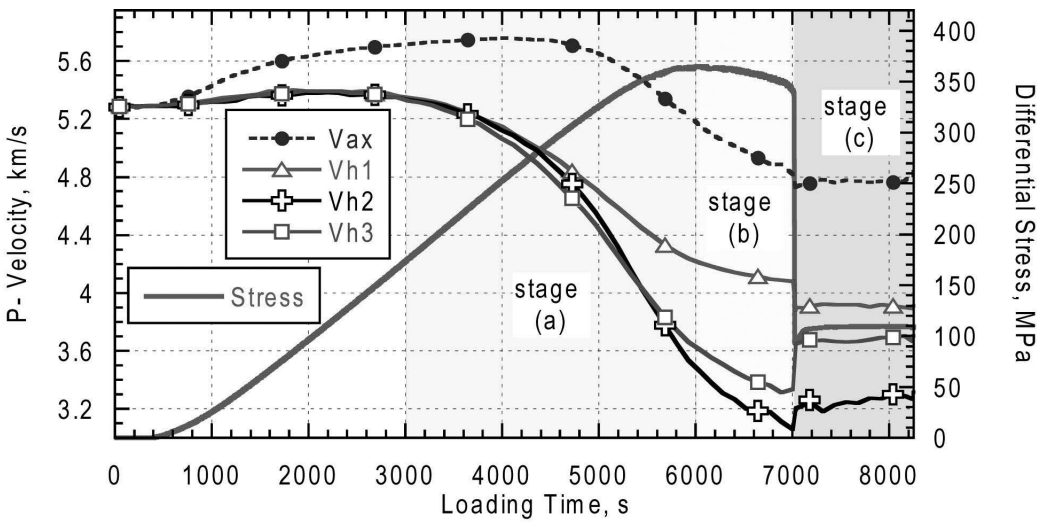
P- Velocity, km/s
Differential Stress, MPa
Loading Time, s
Vax
Vh1
Vh2
Vh3
Stress
stage (a)
stage (b)
stage (c)
5.6
5.2
4.8
4.4
4
3.6
3.2
400
350
300
250
200
150
100
50
0
0
1000
2000
3000
4000
5000
6000
7000
8000

Figure 4 BW

a.)

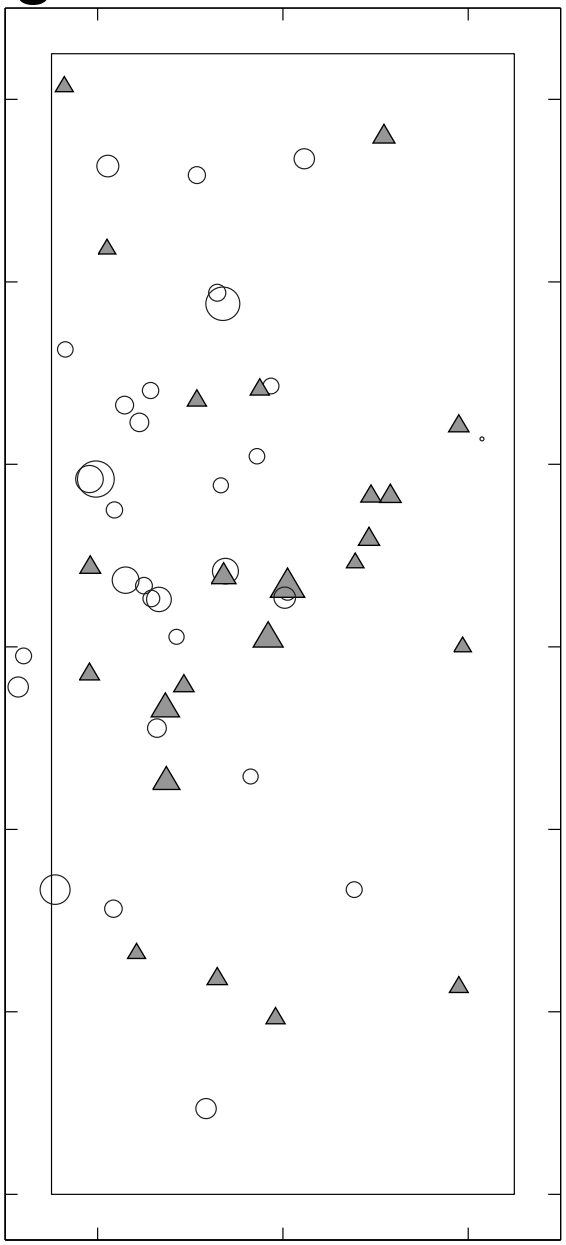

b.)

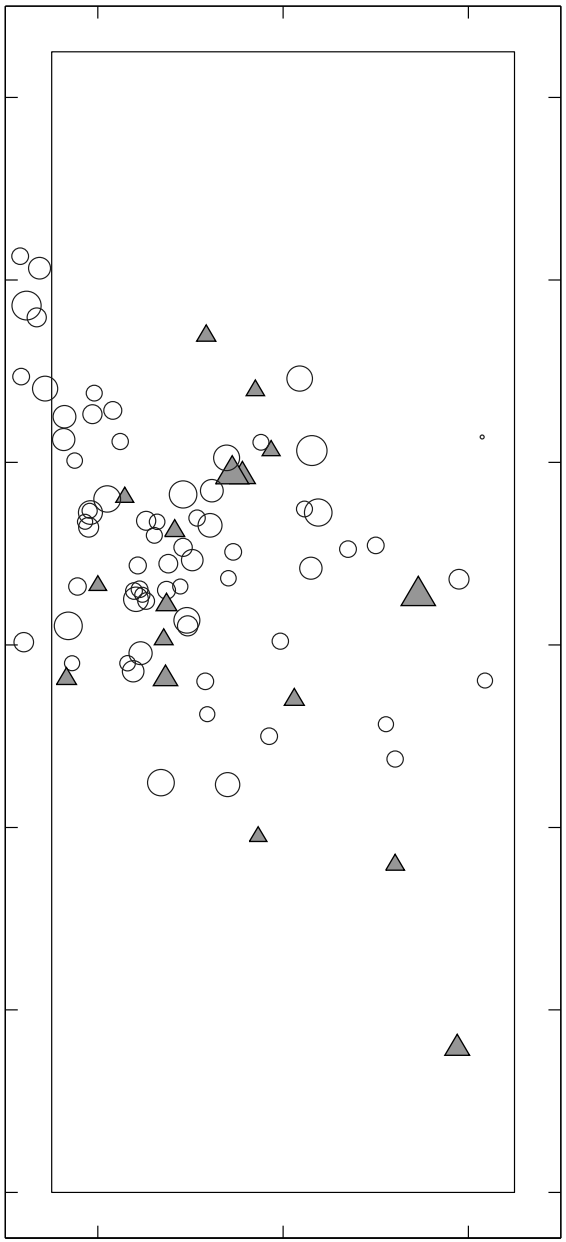

c.)

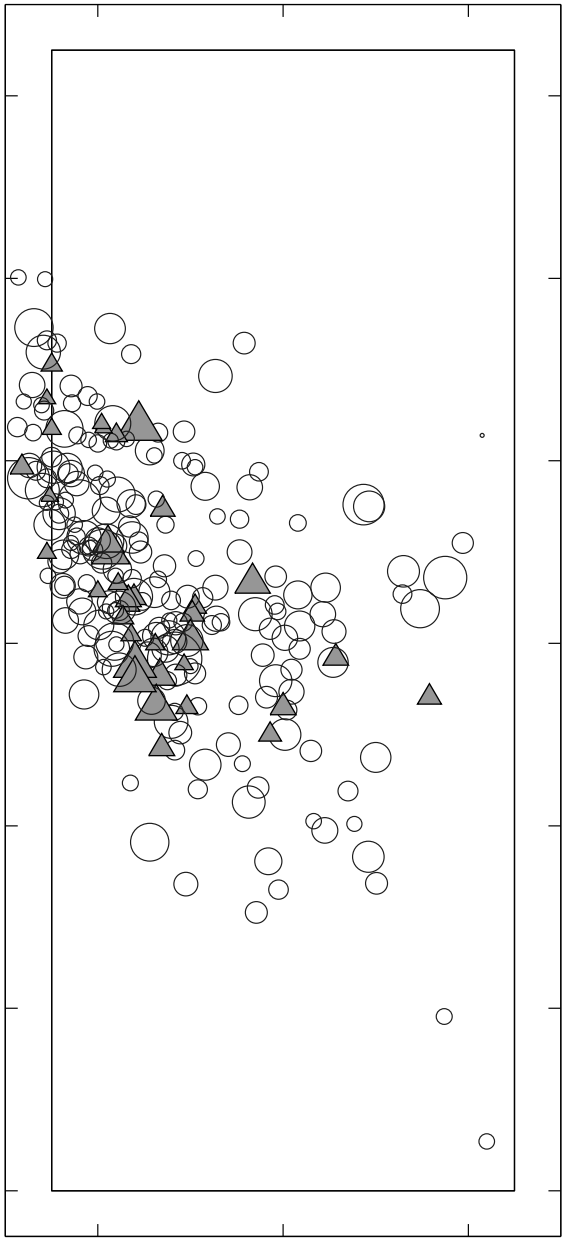

Figure 5 BW

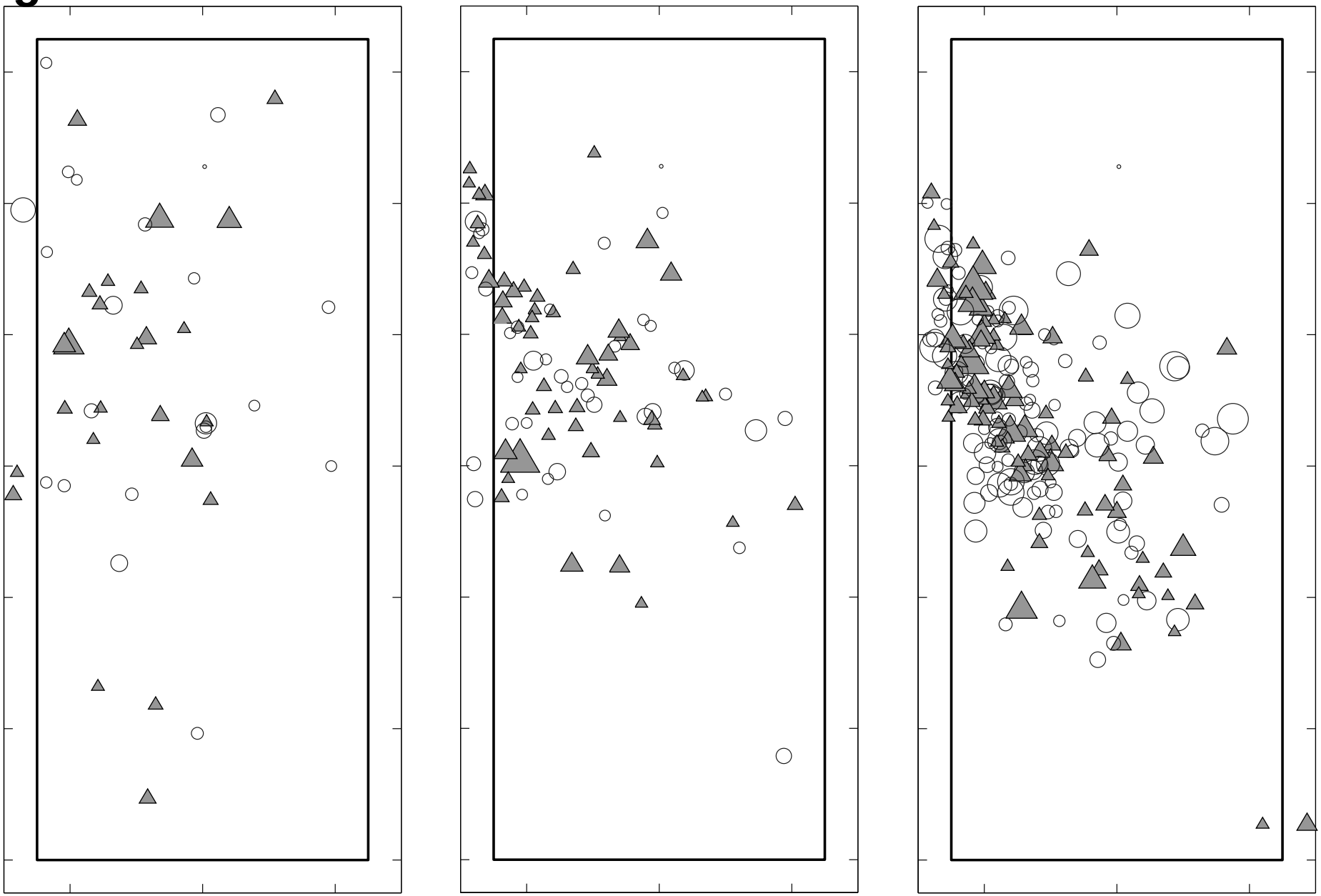

Figure 6 BW

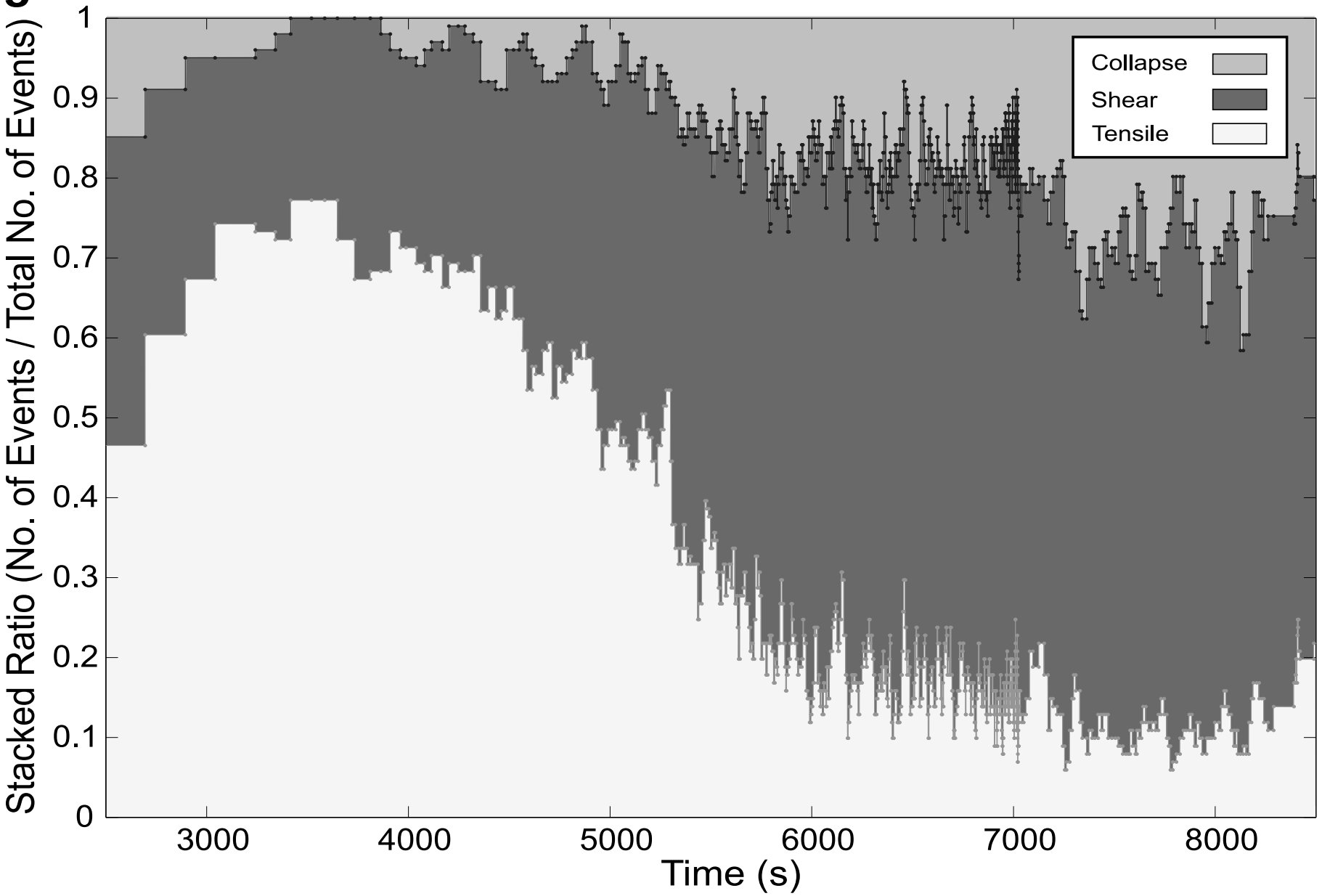
Collapse
Shear
Tensile
Stacked Ratio (No. of Events / Total No. of Events)
Time (s)
0
0.1
0.2
0.3
0.4
0.5
0.6
0.7
0.8
0.9
1
3000
4000
5000
6000
7000
8000

Figure 7 BW

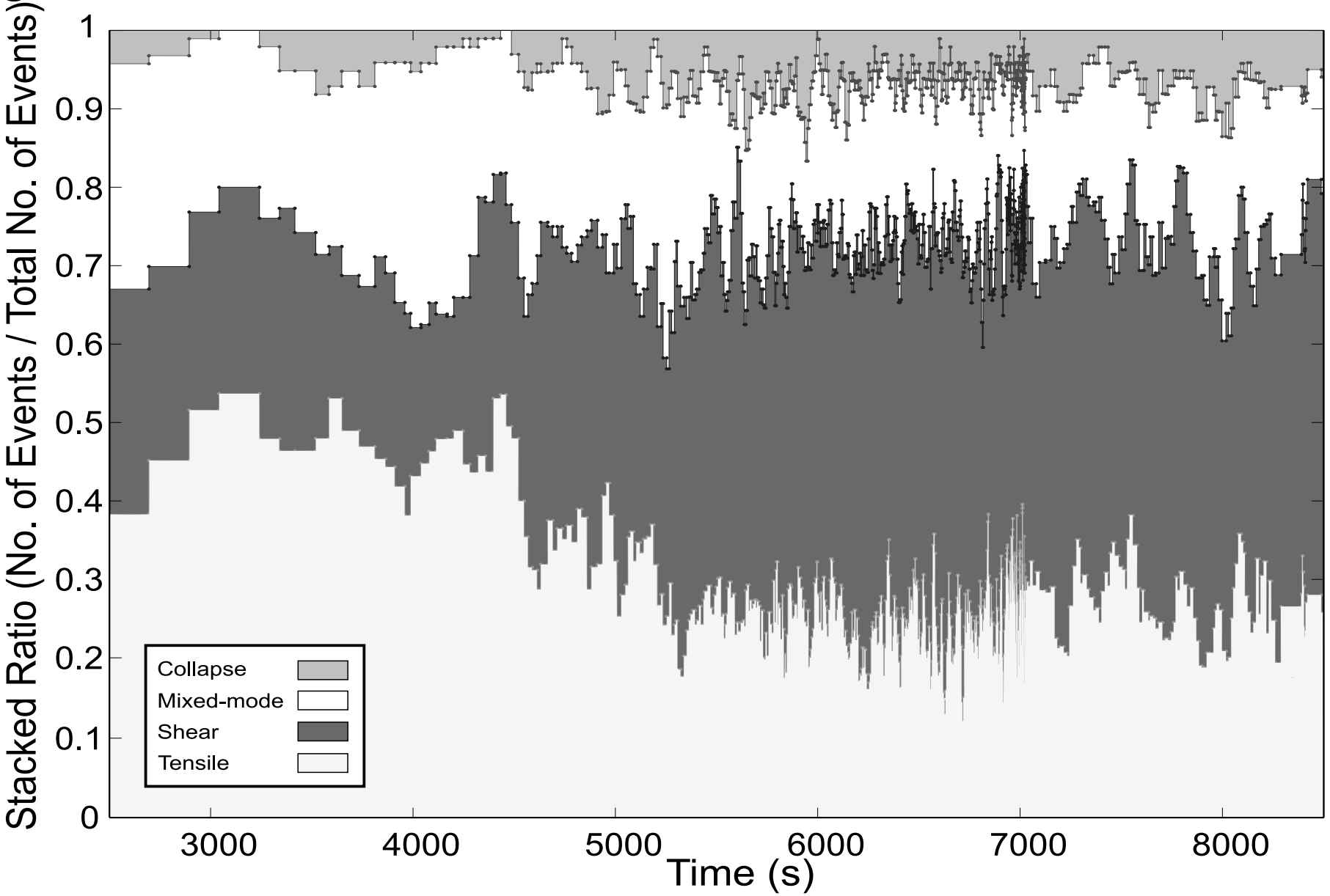
Stacked Ratio (No. of Events / Total No. of Events)
1
0.9
0.8
0.7
0.6
0.5
0.4
0.3
0.2
0.1
0
3000
4000
5000
6000
7000
8000
Time (s)
Collapse
Mixed-mode
Shear
Tensile

Figure 8 BW

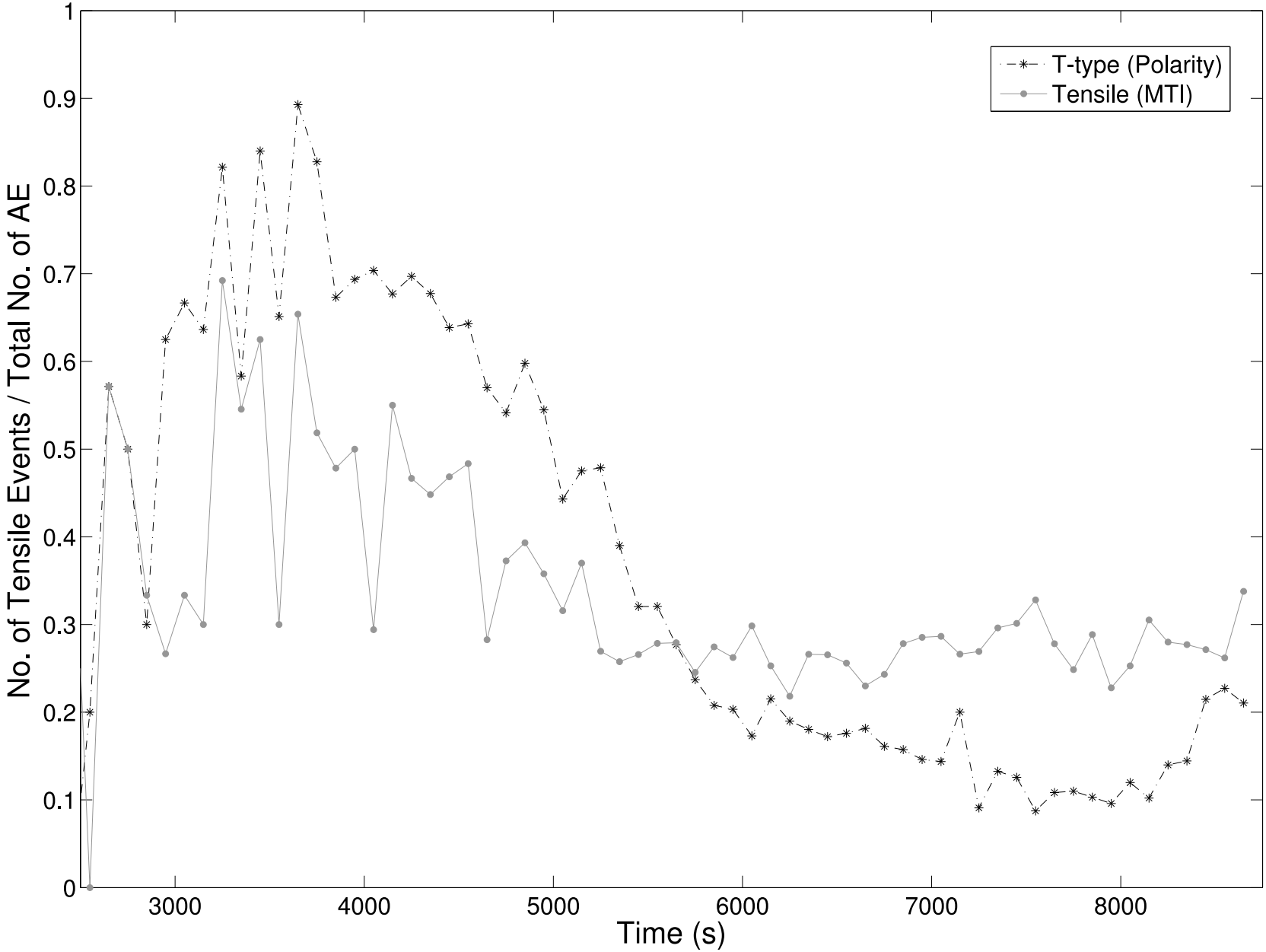
T-type (Polarity)
Tensile (MTI)
No. of Tensile Events / Total No. of AE
Time (s)
0
0.1
0.2
0.3
0.4
0.5
0.6
0.7
0.8
0.9
1
3000
4000
5000
6000
7000
8000

Figure 9 BW

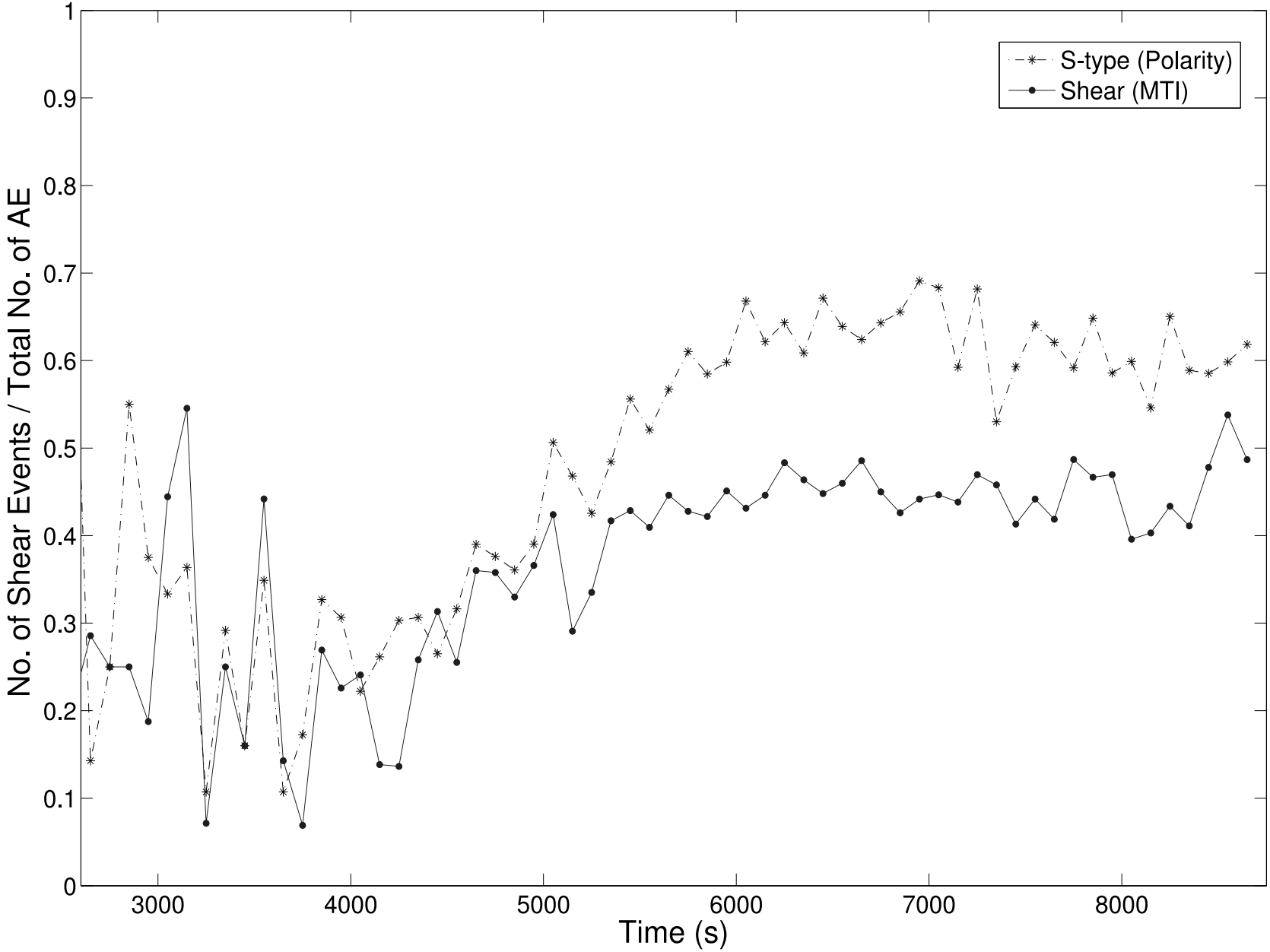
S-type (Polarity)
Shear (MTI)
No. of Shear Events / Total No. of AE
Time (s)
0
0.1
0.2
0.3
0.4
0.5
0.6
0.7
0.8
0.9
1
3000
4000
5000
6000
7000
8000